LANGMUIR

pubs.acs.org/Langmuir Article

Mechanism and Application of Surface-Charged Ferrite Nanozyme-Based Biosensor toward Colorimetric Detection of L-Cysteine

Hongjiao Wu, Jun Liu, Zhuoyu Chen, Pengcheng Lin,* Wentao Ou, Zian Wang, Wei Xiao,* Ying Chen, and Donglin Cao*

Cite This: *Langmuir* 2022, 38, 8266−8279 Read Online

ACCESS | Metrics & More | Article Recommendations | Supporting Information

ABSTRACT: Peroxidase-like nanozymes with robust catalytic capacity and detection specificity have been proposed as substitutes to natural peroxidases in biochemical sensing. However, the catalytic activity enhancement, detection mechanism, and application of nanozyme-based biosensors toward L-cysteine (L-Cys) detection still remain significant challenges. In this work, a doped ferrite nanozyme with well-defined structure and surface charges is fabricated by a two-step method of continuous flow coprecipitation and high-temperature annealing. The resulted ferrite nanozyme possesses an average size of 54.5 nm and a zeta-potential of 6.45 mV. A high-performance biosensor is manufactured based on the peroxidase-like catalytic feature of the doped ferrite. The ferrite nanozyme can oxidize the 3,3′,5,5′-tetramethylbenzidine (TMB) with the assistance of H_2O_2 because of the instinctive capacity to decompose H_2O_2 into ·OH. The Michaelis−Menten constants (0.0911 mM for TMB, 0.140 mM for H_2O_2) of the ferrite nanozyme are significantly smaller than those of horseradish peroxidase. A reliable colorimetric method is established to selectively analyze L-Cys via a facile mixing-and-detecting methodology. The detection limit and linear range are 0.119 μM and 0.2−20 μM, respectively. Taking the merits of the ferrite nanozyme-based biosensors, the L-Cys level in the human serum can be qualitatively detected. It can be anticipated that the surface-charged ferrite nanozyme shows great application prospects in the fields of bioanalytical chemistry and point-of-care testing.

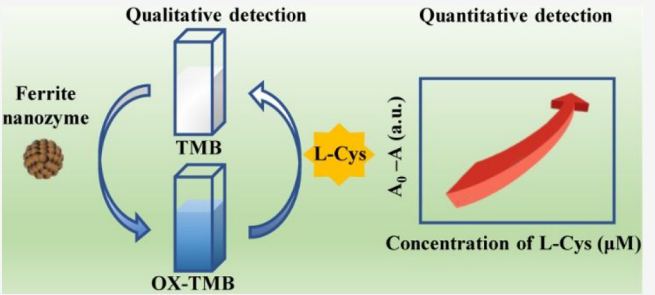

INTRODUCTION

Natural enzymes including nucleic acids, proteins, and other biomacromolecules not only play a significant role in biological activities but also their purified extract is widely used in the fields of molecular detection, biochemical reaction, and tumor treatment.[1−4] However, natural enzymes have inherent shortcomings. Subject to expensive instruments and labor, the purification and extraction of natural enzymes cost a lot. The poor thermal stability makes it difficult to transport and store.[5−7] Researchers are committed to exploiting efficient substitutes for natural enzymes to promote specific biochemical reactions. In 2007, Yan's group took the lead in discovering that Fe_3O_4 nanoparticles can simulate the catalytic behavior of natural enzymes.[8] In 2013, researchers first proposed the concept of nanozymes.[9,10] Nanozymes fully make up for some shortcomings of natural enzymes. They present the advantages of low cost, high stability, and massive production. Because of the development of nanotechnology, biotechnology, and catalytic mechanism, researchers have obtained a deeper understanding of nanozymes. In addition to the magnetic Fe_3O_4 nanoparticles, other kinds of materials also possess enzyme-like catalytic properties, including but not limited to iron-based materials,[11,12] precious-metal materials,[13,14] carbon-based materials,[15,16] metal sulfides,[17,18] metal−organic frameworks, and so on.[19,20] At present, the enzyme-like properties of nanozymes have expanded from peroxidase-like properties[21,22] to catalase-like,[23−25] oxidase,[26,27] superoxide dismutase,[28−31] lactic acid enzyme,[32] and other different properties.

Among various nanozymes, peroxidases are most widely used to detect hydrogen peroxide, glucose, cholesterol, glutathione, and other macromolecules in body fluids.[32−37] As a substitute of natural enzymes, most peroxidase-like nanozymes follow a similar catalytic mechanism. The complex valence states of nanozymes are considered to be an important reason for its ability to simulate the catalytic behavior of natural enzymes. Specifically, the catalytic mechanism of peroxidase-like nanozyme shows the characteristics of Michaelis−Menten kinetics.[38,39] Furthermore, there are mainly two strategies for the detection of the biological molecules (glucose, urea, cholesterol, glutathione, tyrosine, ascorbic acid, etc.), namely the one-step detection and the cascade detection. In the first

Received: March 15, 2022
Revised: June 9, 2022
Published: June 24, 2022

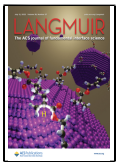

https://doi.org/10.1021/acs.langmuir.2c00657
Langmuir 2022, 38, 8266−8279

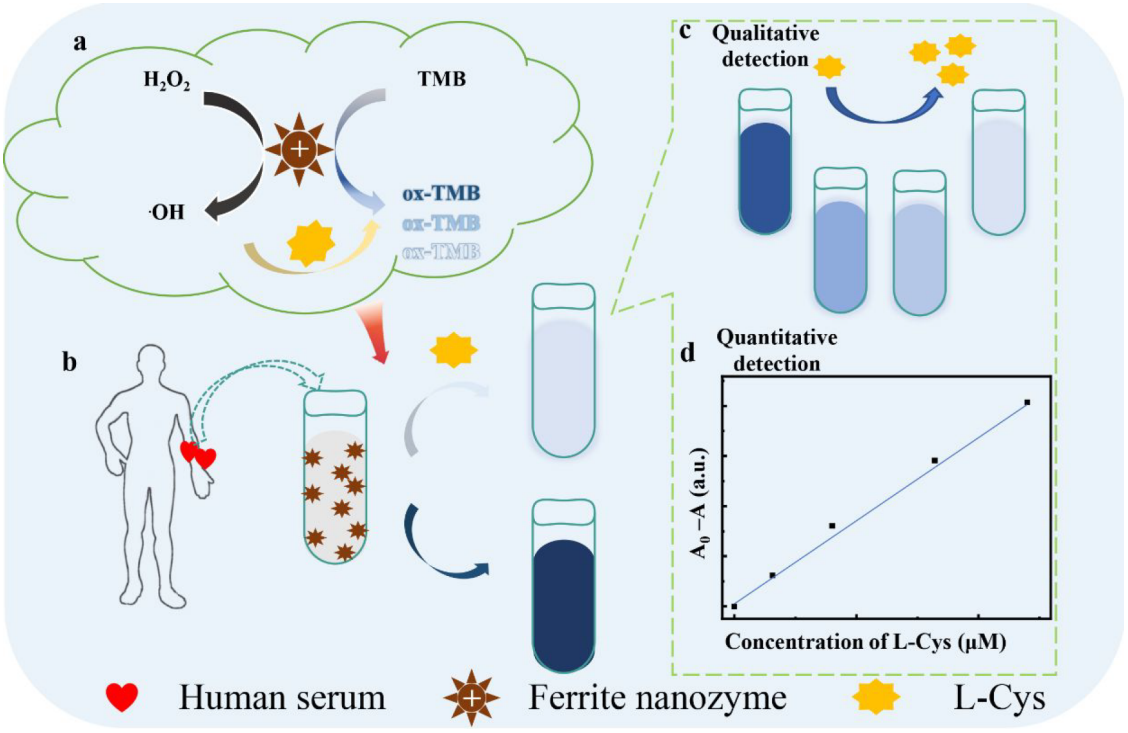

Figure 1. Concept, mechanism, and application of the colorimetric analysis of the L-Cys based on the ferrite-catalyzed biochemical reaction. (a) Mechanism of the colorimetric detection of the L-Cys including the oxidation reaction between H_2O_2 and TMB catalyzed by the peroxidase-like ferrite nanozymes to generate the blue ox-TMB and the L-Cys triggered reduction reaction to generate the colorless TMB. (b) Schematic procedure of the colorimetric analysis of the L-Cys in the real serum samples based on the turnoff absorption of the ferrite-catalyzed biochemical reaction. (c) Visual and qualitative detection of L-Cys according to gray difference when adding different L-Cys dosages. (d) Quantitative sensing of L-Cys based on the linear calibration plot between the L-Cys concentration and the absorbance.

mode, the detection principle is based on the absorption turnoff at about 652 nm (450 or 413 nm) in the detection system consisting of peroxidase-like nanozyme, oxidant hydrogen peroxide, the chromogenic agent TMB (OPD or ABTS),[40] and the reductive biomolecules to inhibit the oxidation reaction in the detection systems.[17,41] When the concentrations of peroxidase-like nanozyme, hydrogen peroxide, and chromogenic agent are set to be fixed values, the concentrations of target detectors and the absorbance can form a linear equation toward the quantitative detection of unknown samples. In the second mode, the detection principle is based on the generation of hydrogen peroxide in the oxidation reaction between oxidase and the target detectors (glucose, uric acid, cholesterol, etc.) and followed by the absorption turnoff at about 652 nm (450 or 413 nm) in the detection system consisting of peroxidase-like nanozyme, the generated hydrogen peroxide, and the TMB (OPD or ABTS).[42,43] When the concentrations of oxidase, peroxidase-like nanozyme, and the chromogenic agent are set to be fixed values, the concentrations of target detectors and the absorbance at about 652 nm (417 or 413 nm) can form a linear equation toward the quantitative detection of unknown samples.

L-Cys plays a highly valuable role in detoxification and metabolism, and its deficiency leads to slow cell proliferation, liver injury, hair discoloration, and malabsorption syndrome.[44−46] Meanwhile, L-Cys can generate disulfide bonds in biological tissues, which is necessary for the formation of protein secondary structure.[47] Therefore, the accurate sensing of L-Cys under physiological conditions is significant to evaluate human health. Previously, a variety of nanozymes (reduced graphene oxide derivative,[37] Fe_3O_4 magnetic nanoparticles,[47] nickel oxide nanoflowers,[48] $CuMnO_2$ nanoflakes,[49] cobalt sulfide nanosheets,[50] vanadium tetrasulfide,[51] CeO_2/CoO,[52] MoS_2−Au@Pt,[53] and Cu@Au(Ag)/Pt[54]) have been exploited to detect the L-Cys concentration. However, the limit of detection (LOD) or the linear range of most nanozymes is generally at relatively high levels. Furthermore, the detailed mechanism in the L-Cys biosensing is seldom discussed because of the lack of comprehensive verification methods and the unclear structure−activity relationship between peroxidase-like nanozyme and the detection reaction path. Therefore, the catalytic activity enhancement, detection mechanism, and application of nanozyme-based biosensors toward L-cysteine (L-Cys) detection still remain significant challenges.

Inspired by the iron-based nanozymes with high catalytic activity, high biocompatibility, and low-cost feature,[55−58] a ferrite nanozyme with well-defined structure and surface charge is fabricated by a facile method. The ferrite nanocrystals are revealed to possess peroxidase-like attributes (Figure 1a). Furthermore, the positive surface charges caused by the Cu^{2+} and Mn^{2+} codoping can inhibit the aggregation of the ferrite nanocrystals, thus leading to low Michaelis−Menten constants (K_m). Afterward, a label-free colorimetric detection approach is conducted to visually detect the trace L-Cys by one-pot biosensing (Figure 1b). The turn-off mechanism in the TMB−H_2O_2−ferrite nanozyme−L-Cys system is confirmed to be the reduction of ·OH and ox-TMB by L-Cys. Importantly, the ferrite nanozyme-based sensing platform is proved to be highly efficient in the qualitative and quantitative detection of low concentration L-Cys in real serum samples (Figure 1c,d).

https://doi.org/10.1021/acs.langmuir.2c00657
Langmuir 2022, 38, 8266−8279

MATERIALS AND METHODS

Materials. Manganese chloride terahydrate ($MnCl_2·4H_2O$, AR) and isopropanol (IPA) were purchased from Damao Chemical Reagent Co., Ltd. 5,5-Dimethyl-1-pyrroline-*N*-oxide (DMPO, 99%) and iron chloride hexahydrate ($FeCl_3·6H_2O$, 99%) were purchased from Macklin. Copper chloride dihydrate ($CuCl_2·2H_2O$, AR), homocysteine (Hcy), ascorbic acid (AA), arginine (Arg), uric acid (UA), hemin, glutamine (GSH), and L-Cys were purchased from Macklin. 3,3′,5,5′-Tetramethylbenzidine (TMB), sodium hydroxide (NaOH, 99.99%), hydrogen peroxide (H_2O_2, 30 wt %), and disodium terephthalate (Na_2TA, HPLC) were purchased from Aladdin. HAc-NaAc buffer solution was purchased from Haibiao Technology Co., Ltd. Serum samples were provided by the Guangdong Second Provincial General Hospital.

Synthesis of Ferrite Nanozyme. Ferrite nanozyme was synthesized by a two-step process of chemical coprecipitation and thermal annealing. Typically, 1.649 g of $MnCl_2·4H_2O$, 1.421 g of $CuCl_2·2H_2O$, and 9.01 g of $FeCl_3·6H_2O$ were synchronously dissolved in 100 mL of deionized water under vigorous stirring to obtain a uniform precursor solution. 1.66 g of NaOH was mixed with 100 mL of deionized water to form a precipitating agent. The precipitating agent was injected into the precursor solution (2 mL min^{-1}) to initiate the coprecipitation reaction. The precursor solution and precipitating agent were mixed in a sample vial under vigorous stirring at a speed of 700 rpm. The whole mixing process lasted for 1 h before the reaction was terminated. The obtained mixtures were purified by washing with deionized water to eliminate residual reactants and followed by drying at 120 °C to remove the water. The final ferrite nanozyme was obtained by thermal annealing the above crude product at 600 °C (heating rate 10 °C min^{-1}) for 120 min in a muffle furnace (Hefei Kejing, KSL-1400X-A1) in an air atmosphere.

Peroxidase-like Catalytic Activity Characterization. The ferrite nanozyme powder was mixed with the HAc−NaAc buffer solution (200 mM, pH 3.6) and followed by treatment in a sonication apparatus (FUYANG-030S, 180 W, 40 kHz) under an ice bath for 40 min to obtain the nanozyme dispersion. The peroxidase mimicking capacity of ferrite nanozyme was tested via the catalytic conversion of colorless TMB into blue oxidized TMB (ox-TMB) with the assistance of H_2O_2. The generation of the ox-TMB can be dynamically monitored by recording the real-time absorbance at 652 nm. Typically, 1110 μL of HAc−NaAc buffer solution (200 mM, pH 3.6), 200 μL of TMB solution (final concentration 0.1 mM), 600 μL of H_2O_2 solution (final concentration 0.3 mM), and 100 μL of nanozyme dispersion (final concentration 50 mg L^{-1}) were successively added into a centrifugal tube and followed by homogeneous mixing at 25 °C, unless otherwise stated. The concentration and pH-dependent catalytic behaviors were studied by changing the pH and nanozyme concentration in the catalytic system.

Measuring the ·OH by Fluorescence Spectrometer. The ·OH produced from the ferrite-catalyzed H_2O_2 decomposition was evaluated by monitoring the fluorescence (FL) change of 2-hydroxy disodium terephthalate (Na_2TAOH) generated through the oxidizing of disodium terephthalate (Na_2TA). In brief, the hydroxyl radical can oxidize Na_2TA to form Na_2TAOH with a characteristic FL peak at 440 nm when excited by a UV light of 315 nm. The HAc−NaAc buffer solutions (pH = 3.6, 200 mM) containing (a) only Na_2TA, (b) Na_2TA and H_2O_2, (c) Na_2TA, H_2O_2 and nanozymes, (d) nanozymes and Na_2TA, and (e) nanozymes and H_2O_2 were reacted for 24 h. Then, the fluorescence spectra were recorded. The final concentrations of Na_2TA, H_2O_2, and ferrite nanozymes were set to be 0.5 mM, 1 mM, and 50 mg L^{-1}, respectively.

Investigation of the Nanozyme Activity through Scavenging ·OH. It is well-established that hydroxyl radicals have been regarded as active intermediates, which can be scavenged by IPA. The typical process was performed as follows: adding different volumes (0, 400, 600, and 800 μL) of IPA to a mixture containing 20 μL of TMB solution (10 mM), 200 μL of H_2O_2 solution (10 mM), and 100 μL of nanozyme dispersion (1 mg mL^{-1}) and finally adding a certain amount of acetate buffer until the final total volume was 2 mL. The final concentrations of TMB, H_2O_2, and ferrite nanozyme were set to be 0.2 mM, 1 mM, and 50 mg L^{-1}, respectively. Finally, the UV−vis spectra of the catalytic reactions were recorded.

Steady-State Kinetic Assays of the Nanozyme. Steady-state kinetic analysis was performed by recording the real-time absorbance of ox-TMB at 652 nm (ε_{652nm} = 39000 M^{-1} cm^{-1}). The detailed process was conducted by mixing 100 μL of nanozyme dispersion (final concentration 50 mg L^{-1}), 1110 μL of buffer solution (200 mM HAc-NaAc, pH 3.6, 25 °C), 200 μL of TMB solution (final concentration 0.1 mM) as substrate, different volumes of H_2O_2 solution (final concentration from 0 to 0.8 mM) or 200 μL of H_2O_2 solution (final concentration 0.3 mM) as substrate, and different volumes of TMB solution (final concentration from 0 to 0.1 mM), unless otherwise stated. Accordingly, the oxidation rates of TMB by H_2O_2 were analyzed in terms of the Michaelis−Menten model.

Measurement of L-Cys Using the Nanozyme-Based Biosensor. The measurement procedure of L-Cys was listed as follows: (1) adding TMB solution, H_2O_2 solution, and nanozyme dispersion into a 2 mL of centrifuge tube successively, then adding L-Cys solution with different concentrations (the final concentrations varying from 0 to 20 μM) as the samples to be tested, and finally adding HAc−NaAc buffer solution to a final total volume of 2 mL; (2) putting the centrifuge tube on a mixer with a rotating speed of 1000 rpm and mixing for 10 min, then putting the centrifuge tube on a palm centrifuge, and centrifuging for 5 min at a rotating speed of 5000 rpm; (3) collecting the supernatant and placing it in a spectrophotometer for absorbance detection. The final concentrations of TMB, H_2O_2, and nanozymes in the L-Cys detection system were set to be 0.1 mM, 1 mM, and 50 mg L^{-1}, respectively.

Verification of the Turnoff Mechanism of L-Cys in the Ferrite Nanozyme−Hydrogen Peroxide−TMB System. The experiment was divided into two parts to verify two possible turnoff mechanisms of L-Cys in the ferrite nanozyme−hydrogen peroxide−TMB system; the detailed procedures are as follows. In the first part, 100 μL of enzyme dispersion, 1580 μL of buffer solution, 200 μL of hydrogen peroxide solution, and 20 μL of TMB solution were mixed in a centrifuge tube (A) for 60 min to realize the complete oxidation of TMB and then transferred to a cuvette to measure the absorbance at 652 nm with a spectrophotometer. Afterward, 100 μL of L-Cys solution (0.4 mM) was mixed with the above solution for 1 min. The absorbance at 652 nm was immediately measured again with a spectrophotometer. In the second part, two groups of mutually controlled experiments were designed to verify whether L-Cys reacts with hydroxyl radical: (1) First, 100 μL of enzyme dispersion, 1580 μL of buffer solution, and 200 μL of hydrogen peroxide solution were mixed in two centrifuge tubes (B and C) for 10 min. (2) Second, 100 μL of buffer solution (200 mM) and 100 μL of L-Cys solution (2 mM) were added into tube B and tube C, respectively and were fully mixed for 15 min. (3) Lastly, 20 μL of TMB solution was added into tubes B and C and followed by measuring the absorbance at 652 nm. The final concentrations of TMB, H_2O_2, and nanozymes in the above experiments were set to be 0.1 mM, 1 mM, and 50 mg L^{-1}, respectively.

Detection of Hydroxyl Radical Elimination by Electron Paramagnetic Resonance (EPR). Hydroxyl radicals were trapped by DMPO and detected by electron paramagnetic resonance spectroscopy (EPR, Bruker EMXplus-10/12 spectrometer). The HAc−NaAc buffer solutions (pH = 3.6, 200 mM) include (a) H_2O_2 + ferrite nanozyme, (b) H_2O_2 + ferrite nanozyme + L-Cys, and (c) only H_2O_2 which were reacted for 5 min. Then, the above solutions were immediately mixed with 2 μL of DMPO. Finally, the mixtures were transferred into a capillary tube for EPR measurements. The final concentrations of H_2O_2, nanozyme, and L-Cys were set to be 0.5 M, 0.5 mg mL^{-1}, and 5 μM, respectively.

Analysis of L-Cys in Serum Samples Using the Nanozyme-Based Biosensor. L-Cys detection was conducted by the following procedure: (1) TMB solution (10 mM), H_2O_2 solution (10 mM), ferrite nanozyme dispersion (50 mg L^{-1}), and acetate buffer solution (pH 3.6) were prepared. The serum sample was diluted 10 times with the buffer to obtain the sample to be tested. (2) 20 μL of TMB solution, 200 μL of H_2O_2 solution, 100 μL of ferrite nanozyme dispersion, and

https://doi.org/10.1021/acs.langmuir.2c00657
Langmuir 2022, 38, 8266−8279

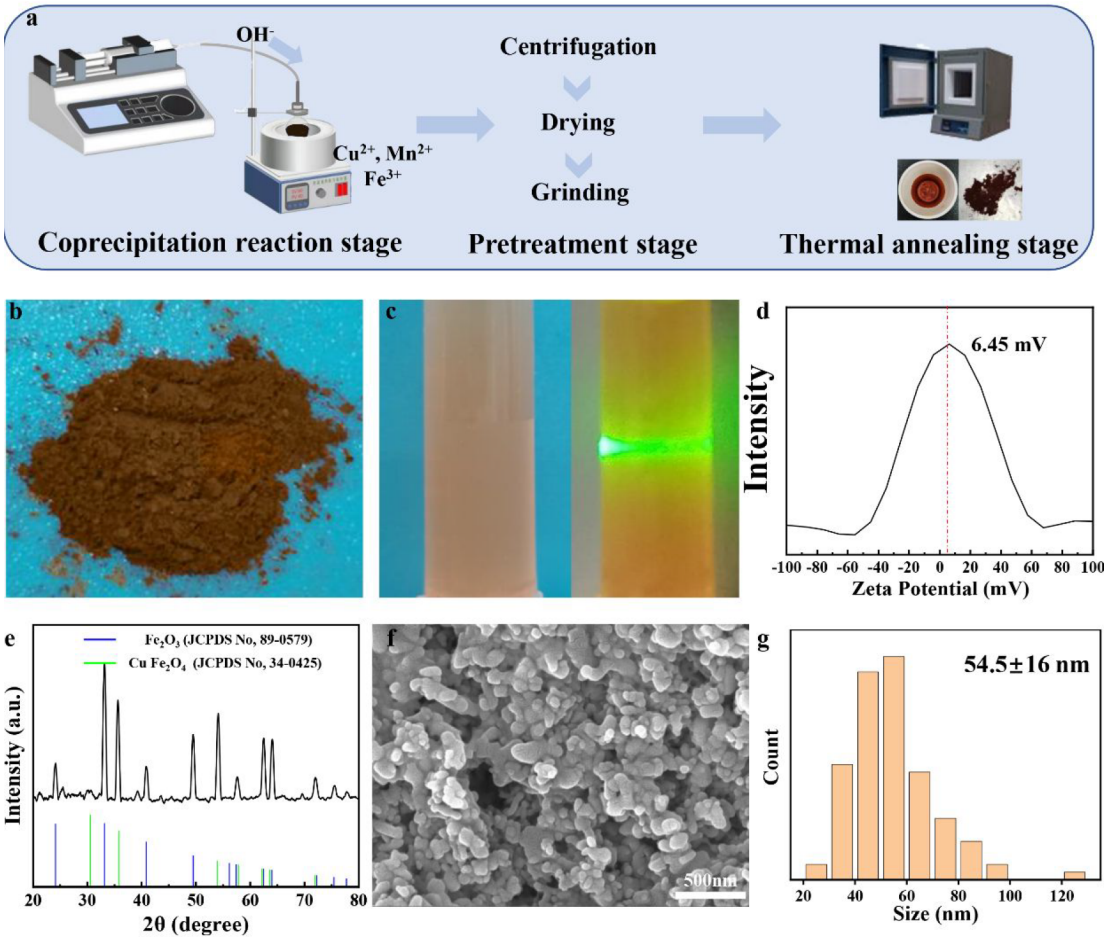

Figure 2. Preparation and basic characterization of the ferrite nanozyme. (a) Experimental setup for the preparation process of the ferrite nanozyme, mainly including the chemical coprecipitation and the thermally annealed reaction. (b) Digital image of the as-prepared ferrite nanozyme. (c) Photograph of the ferrite nanozyme dispersed in aqueous phase and the corresponding Tyndall effect of the ferrite nanozyme dispersion. (d) Zeta-potential of the ferrite nanozyme dispersion. (e) XRD pattern of the ferrite nanozyme powder (black) and the standard XRD pattern of Fe_2O_3 nanocrystals (JCPDS Card No. 89e0579) (blue) and ferrite $CuFe_2O_4$ (JCPDS Card No. 34e0425) (green). (f, g) SEM image and the particle size of the ferrite nanozyme.

100 μL of serum samples were added into a centrifuge tube successively; finally the buffer solution was added to a total volume of 2 mL. (3) The centrifuge tube was put on a mixer with a rotating speed of 1000 rpm and mixed for 10 min, and then the centrifuge tube was put in a palm centrifuge and centrifuged for 5 min at a rotating speed of 5000 rpm. (4) The supernatant was collected and placed it in a spectrophotometer for absorbance detection.

Instrument and Characterization. The micromorphology and lattice fringe of the ferrite nanozyme were recorded by transmission electron microscope (TEM) (JEM-2100F, Japan). The surface morphology and particle size of the ferrite nanozyme were investigated by scanning electron microscopy (SEM) (Zeiss Sigma 300, Germany). An X-ray photoelectron spectroscopy (XPS) (Thermo ESCALAB 250Xi, USA) measurement was conducted to determine the hybrid compositions and the bonding configurations of the ferrite nanozyme. X-ray diffraction (XRD) (Bruker AXS, Germany) was used to examine the crystal structure of the ferrite nanozyme. The UV−vis spectra of the catalytic reactions were obtained by using a spectrophotometer (Lengguang, China). Fluorescent spectra were collected by a fluorescence spectrometer (Varian FLR025, USA). The zeta-potentials of nanozyme and binary nanozyme−TMB were tested by the zeta-potential instrument (Beckman Coulter, USA).

RESULTS AND DISCUSSION

Structural and Composition Analysis of Ferrite Nanozyme. The detailed procedure of the ferrite nanozyme fabrication is shown in Figure 2a. In this work, the continuous flow injection and dynamic chemical coprecipitation are synergistically utilized to synthesize the ferrite precursors and followed by the thermal annealing to obtained the ferrite nanozyme. The sodium hydroxide aqueous solution is independently injected into a closed reactor containing a ternary aqueous solution of $MnCl_2$, $CuCl_2$, and $FeCl_3$ and violently mixed to initiate the chemical coprecipitation between the metal cations (Mn^{2+}, Cu^{2+}, and Fe^{3+}) and the OH^- (eq 1). The purified metal hydroxide precipitates are ground and then thermally annealed to form the Mn^{2+} and Cu^{2+} codoped ferrite nanocrystals (eq 2).

$$x\mathrm{Cu}^{2+} + y\mathrm{Mn}^{2+} + z\mathrm{Fe}^{3+} + \left(2x + 2y + 3z\right)\mathrm{OH}^- \xrightarrow{\text{coprecipitation}} x\mathrm{Cu(OH)_2} + y\mathrm{Mn(OH)_2} + z\mathrm{Fe(OH)_3} \quad (1)$$

$$\mathrm{Cu(OH)_2} + \mathrm{Mn(OH)_2} + \mathrm{Fe(OH)_3} \xrightarrow{\text{thermal annealing}} \text{ferrite nanozyme} \quad (2)$$

The Mn^{2+} and Cu^{2+} codoped ferrite presents a brown appearance under white light irradiation (Figure 2b), indicating

https://doi.org/10.1021/acs.langmuir.2c00657
Langmuir 2022, 38, 8266−8279

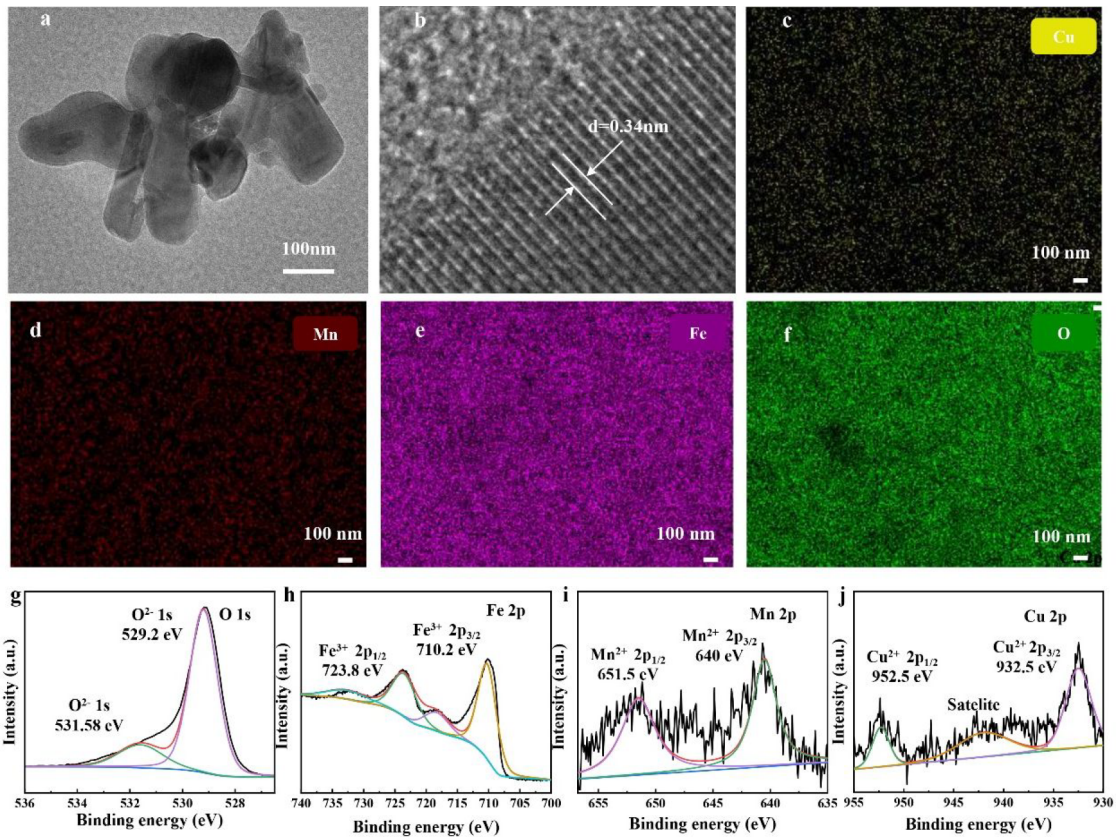

Figure 3. Chemical composition and crystal microstructure of the ferrite nanozyme. (a, b) TEM image and the magnified high-resolution TEM image of the ferrite nanozyme. (c–f) SEM EDS elemental mapping images of Cu, Mn, Fe, and O, respectively. (g–j) XPS spectra of four elements (O, Fe, Mn, and Cu) in the ferrite nanozyme sample.

a significant visible light absorption. After treatment with sufficient ultrasonic dispersion, a homogeneous ferrite dispersion in deionized water was obtained as presented in Figure 2c. When a laser beam (532 nm) passes through the ferrite dispersion, a clear light scattering of the Tyndall effect appeared, thus revealing a typical behavior of colloid. The cation doping also introduces additional charges to the ferrite, which is identified by a zeta-potential of 6.45 mV in Figure 2d. The crystal structure of the Mn^{2+}, Cu^{2+} codoped ferrite is determined by powder XRD. Results in Figure 2e illustrate that the ferrite possesses high crystallinity degree. The diffraction peaks at 2θ = 24.16°, 33.18°, 40.84°, 49.52°, 57.62°, 62.44°, 64.06°, 75.5°, and 77.9° are assigned to the Fe_2O_3 nanocrystals (JCPDS Card No. 89e0579). The diffraction peaks at 2θ = 30.5°, 35.6°, 54.14°, 57.62°, 62.44°, 64.06°, and 71.86° are assigned to the ferrite $CuFe_2O_4$ (JCPDS Card No. 34e0425).

The morphology and microstructure of the Mn^{2+} and Cu^{2+} codoped ferrite are characterized by SEM and TEM. As displayed in Figure 2f, the Mn^{2+} and Cu^{2+} codoped ferrite presents well-defined nanostructure. In addition, the atomic percentages of Fe, O, Mn, and Cu of in the ferrite nanocrystals are tested to be 49.10%, 49.64%, 0.55% ,and 0.71% from the EDX analysis (Figure S1 and Table S1), demonstrating the efficient doping of Mn and Cu in the ferrite nanozyme. The average particle size is calculated to be about 54 nm through statistical calculation via ImageJ and Gaussian fitting via Origin software (Figure 2g). As presented in the TEM image (Figure 3a), Mn^{2+} and Cu^{2+} codoped ferrite possesses a typical flat morphology. The magnified high-resolution TEM image in Figure 3b demonstrates that the clear lattice fringe of ferrite nanocrystal is figured out to be 0.34 nm, and the lattice fringes are highly consistent along a certain direction. The SEM EDS mapping images of the samples in Figure 2f confirm the coexistence and the uniform distribution of O, Fe, Cu, and Mn in the doped nanocrystals (Figure 3c–f). XPS measurement is applied to verify the chemical compositions and the bonding configurations of the ferrite nanozyme. The full spectrum of XPS survey scan shows that the ferrite nanozyme is composed of oxygen, iron, manganese, and copper (Figure S2). Panels g, h, i, and j in Figure. 3 present the O 1s, Fe 2p, Mn 2p, and Cu 2p spectra of the ferrite nanozyme, respectively. The peaks at 529.2 and 531.58 eV originate from the oxygen atoms in the ferrite nanozyme sample (Figure 3g).[59,60] Figure 3h shows the Fe 2p XPS spectrum of ferrite nanozyme sample with two binding energies at 710.2 eV (Fe $2p_{3/2}$) and 723.8 eV (Fe $2p_{1/2}$), which are assigned to Fe^{3+}.[61−63] High-resolution spectra of Mn 2p in ferrite nanozyme are deconvoluted into Mn $2p_{3/2}$ and Mn $2p_{1/2}$, with binding energies at 640.0 and 651.5 eV, respectively (Figure 3i).[64−66] Figure 3j shows the high-resolution XPS spectra of Cu 2p, which are deconvoluted into Cu $2p_{3/2}$ and Cu $2p_{1/2}$, with binding energies at 932.5 and 952.3 eV, respectively.[67−69]

Peroxidase-like Activity of Ferrite Nanozyme. The peroxidase-mimicking behaviors of ferrite nanozyme is investigated by catalyzing the oxidation of TMB. The detailed oxidation reaction is given in eq 3.

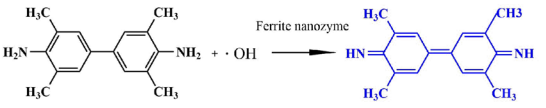

(3)

https://doi.org/10.1021/acs.langmuir.2c00657
Langmuir 2022, 38, 8266−8279

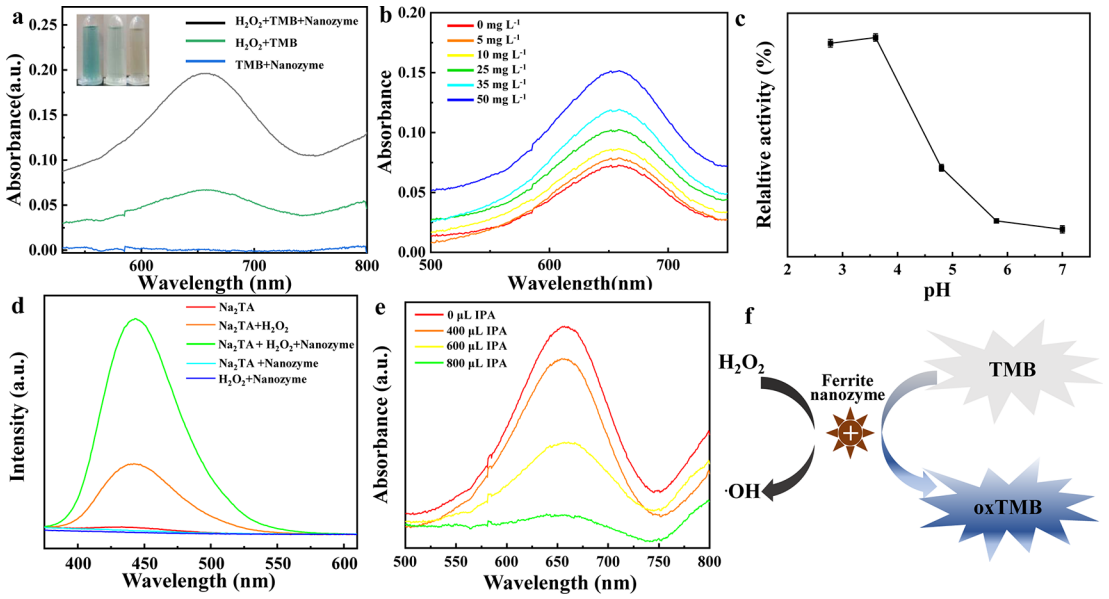

Figure 4. Peroxidase-like activity analysis of ferrite nanozyme. (a) Visible light absorption spectra and the displayed color of different nanozyme catalyzed systems: (1) TMB + ferrite nanozyme, (2) H_2O_2 + TMB, and (3) H_2O_2 + TMB + ferrite nanozyme in buffer solution (pH 3.6) after incubating for 15 min. (b) Visible light absorption spectra of nanozyme-catalyzed systems containing TMB (0.1 mM), H_2O_2 (0.3 mM), and different concentrations of ferrite nanozyme (from 0 to 50 mg L^{-1}). (c) pH-dependent POD activity of the ferrite nanozyme. (d) Fluorescence spectra of different groups including only Na_2TA, Na_2TA + H_2O_2, Na_2TA + H_2O_2 + nanozyme, nanozyme + Na_2TA, and nanozyme + H_2O_2. The final concentrations of Na_2TA, nanozyme, and H_2O_2 are 1 mM, 0.5 mM, and 50 mg L^{-1}, respectively. (e) POD activity of the ferrite nanozyme without and with a hydroxyl radical scavenger in a 2 mL of mixture containing 20 μL of TMB, 200 μL of H_2O_2, and 200 μL of nanozyme dispersion. The final concentrations of TMB, H_2O_2, and nanozymes are 0.2 mM, 1 mM, and 50 mg L^{-1}, respectively. (f) Schematic diagram of nanozyme-catalyzed systems converting the colorless TMB to blue ox-TMB.

The colorless TMB in the detection system can be transformed into a blue oxidized TMB (ox-TMB), possessing a strong light absorption at 652 nm.[70−72] For the detection system containing TMB and ferrite nanozyme, there is no absorption at 652 nm due to the absence of a key reaction substrate (H_2O_2). This phenomenon also reveals the absence of dissolved O_2 in the detection system and the absence of oxidation capacity of the ferrite nanozyme. While for the detection system containing TMB and H_2O_2, there is slight absorption at 652 nm probably on account of the slow oxidation reaction between TMB and ·OH. With the addition of ferrite nanozyme in the TMB−H_2O_2 solution, the color for the ternary mixed system is evolved into deep blue because of the increased generation of ·OH when H_2O_2 and ferrite nanozyme are mixed together. Meanwhile, an enhanced absorbance at 652 nm is determined in the absorption spectrum (Figure 4a), indicating the generation of the blue ox-TMB. The absorption spectra listed in Figure S3 demonstrate that ferrite nanozyme possesses no characteristic absorption peak from 500 to 800 nm. The above results imply that the ferrite nanozyme can efficiently boost the oxidation reaction. Furthermore, the superior peroxidase-like activity of the ferrite enables its application as peroxidase-like artificial enzyme. Generally, the catalytic behaviors of natural enzymes are sensitive to the enzyme concentration and pH. The enzyme concentration (or pH) dependence of the peroxidase enzyme performance is investigated by recording the generation of ox-TMB when only changing the enzyme concentration or pH in the ternary detection system of ferrite nanozyme, TMB, and H_2O_2. Figure S4 shows the color of dispersion containing H_2O_2 and TMB becomes deeper when increasing the concentration of ferrite nanozyme from 0 to 50 mg L^{-1}. The increased absorbance at 652 nm is ascribed to the enhanced catalytic activity in the reaction system (Figure 4b). Thus, we are convinced that the mimicking enzymatic activity of ferrite nanozyme is the catalyst dose dependence. Similarly, Figure S5 shows the changing color of dispersion containing the fixed contents of ferrite nanozyme, TMB, and H_2O_2 along with the increased pH condition from 2.8 to 7. The results in Figure 4c and Table S2 demonstrate the production of ox-TMB at pH = 2.8 is slightly smaller than that at pH = 3.6, whereas the production of ox-TMB presents a dramatic decrease when increasing the pH from 3.6 to 7. It is worth noting that the strongest absorbance at 652 nm is generated at pH = 3.6, revealing the highest activity of the ferrite nanozyme. Thus, concentration of 50 mg L^{-1} and pH of 3.6 are the optimized conditions for the subsequent experiments.

To confirm the generation of ·OH by decomposing the H_2O_2 with the assist of the ferrite nanozyme, a fluorescent probe disodium terephthalate (Na_2TA) is applied to capture ·OH to form disodium 2-hydroxyterephthalate (Na_2TAOH) possessing a characteristic fluorescence emission around 440 nm when excited by UV light of 315 nm. The detailed oxidation reaction is given in eq 4.

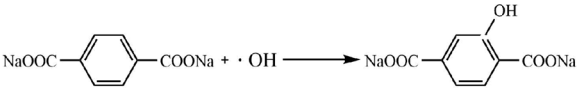

(4)

The detection systems containing only Na_2TA and Na_2TA + ferrite nanozyme show no fluorescence emission around 440 nm when irradiated by UV light of 315 nm due to the absence of H_2O_2. Furthermore, the detection system of containing H_2O_2 demonstrates no fluorescence around 440 nm due to the absence of Na_2TA probe, whereas a mild fluorescence emission appeared in the Na_2TA + H_2O_2 detection system. Finally, the strongest fluorescence emission is presented in the Na_2TA + H_2O_2 + ferrite nanozyme detection system, verifying the generation of ·OH by decomposing the H_2O_2 in the presence

https://doi.org/10.1021/acs.langmuir.2c00657
Langmuir 2022, 38, 8266−8279

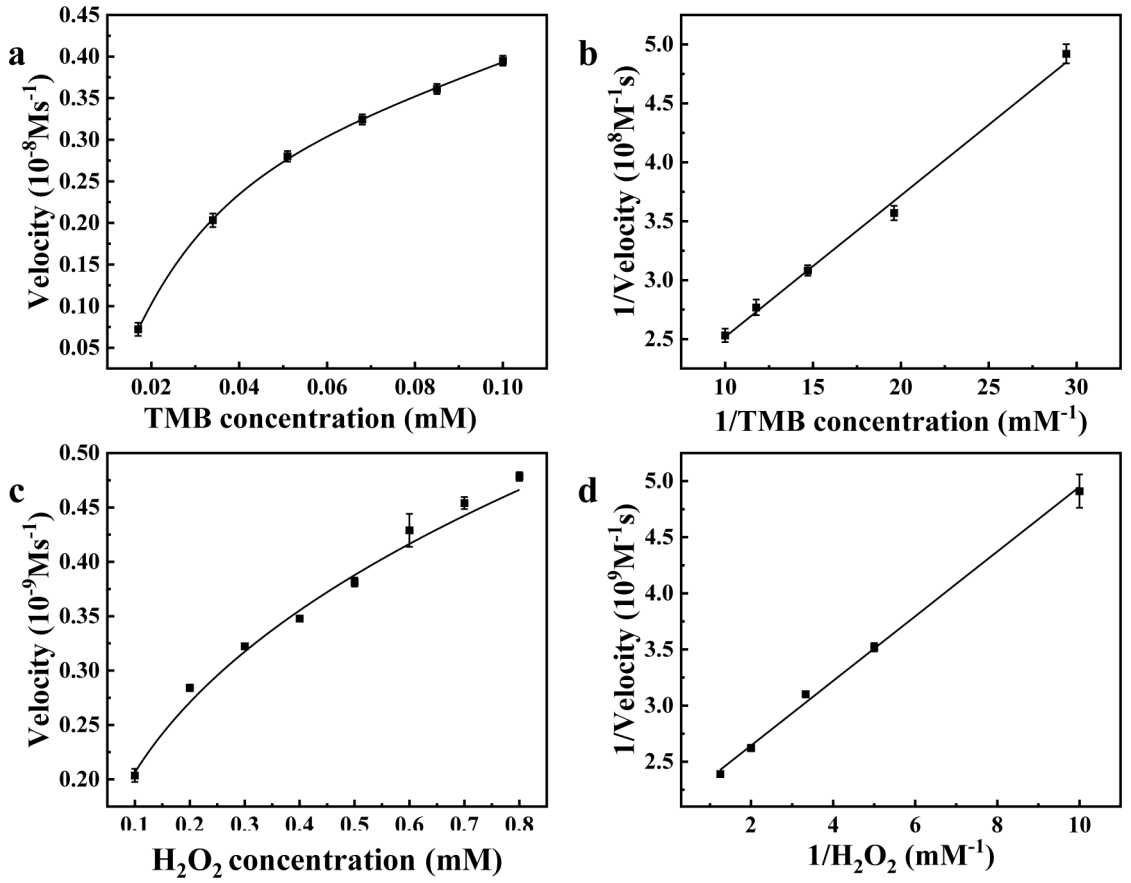

Figure 5. Steady-state kinetic analysis of the ferrite nanozyme (50 mg L^{-1}) at pH 3.6. (a, c) Michaelis−Menten curve of the ferrite nanozyme with TMB substrate (H_2O_2 concentration 0.3 mM, TMB concentrations ranging from 0 to 0.1 mM) or with H_2O_2 substrate (TMB concentration 0.1 mM, H_2O_2 concentrations ranging from 0 to 0.8 mM). (b, d) Double-reciprocal plots of catalytic activity of the ferrite nanozyme.

of the ferrite nanozyme (Figure 4d). To further confirm the function of ·OH in the TMB oxidation process, IPA is selected as a radical scavenger to neutralize the ·OH.[73] Compared to the control without IPA addition, the absorbance of ox-TMB at 652 nm is gradually reduced when increasing the IPA addition from 100 to 800 μL (Figure 4e), proving that ·OH is directly involved in the oxidation process of TMB to produce ox-TMB as shown in Figure 4f.

Catalytic Mechanism of the Ferrite Nanozyme. To deeply analyze the catalytic kinetic behavior of the ferrite nanozyme, the peroxidase-like activity of the ferrite nanozyme together with enzyme kinetics theory is investigated according to eqs 5 and 6.

$$V = \frac{V_{max}[S]}{K_m + [S]} \quad (5)$$

$$\frac{1}{V} = \frac{K_m}{V_{max}}[S] + \frac{1}{V_{max}} \quad (6)$$

where K_m, [S], V, and V_{max} represent the Michaelis constant, substrate concentration, conversion rate of the substrates, and the maximum conversion rate. In accordance with eqs 5 and 6, there is linear relationships between $1/V$ and [S]. Experimentally, the steady-state kinetic calculation is conducted by changing the concentration of TMB or H_2O_2 in the ferrite nanozyme−H_2O_2−TMB systems. As listed in Figure 5a,c, the oxidizing behavior of TMB catalyzed by ferrite nanozyme demonstrates a classical Michaelis−Menten feature when using TMB or H_2O_2 as substrates. Meanwhile, the double-reciprocal plots of catalytic performances for both TMB and H_2O_2 substrates are in accordance with the Lineweaver−Burk equation (Figure 5b,d). The K_m of the ferrite nanozyme for the H_2O_2 substrate is then calculated to be 0.140 mM based on the data in Tables S3 and S4, which is smaller than those of reported peroxidase-like nanozymes and that of HRP (3.7 mM).[74−77] Notably, the K_m value of the ferrite nanozyme for the TMB substrate is 0.0911 mM based on the data in Tables S5 and S6, which is also smaller than that of HRP (0.43 mM).[17,78] The relatively low K_m indicates that the superior affinity between the ferrite nanozyme and H_2O_2 (or TMB), leading to the improved peroxidase-mimicking activity. To figure out the mechanism on the intensive affinity between the ferrite nanozyme and TMB, the zeta-potential analysis of the ferrite nanozyme dispersion is conducted. As listed in Figure 2d, the pristine ferrite nanozyme presents a positive charge (6.45 mV) at pH 3.6. It is worth noting that the zeta-potential of the ferrite nanozyme after combining with TMB shows an increase to 7.37 mV (Figure S6). The increased positive charge is probably ascribed to the phenomenon that the nonoxidized TMB can carry partial positive charge in a weak acid environment (pH 3.6),[17,36] further proving the efficient combination of the ferrite nanozyme and the substrate. The surface charges can inhibit the agglomeration of the nanosized ferrite nanozyme, thus leading to the enlarged specific surface area. Furthermore, the Cu and Mn doping also can strengthen the polarization of the nearby Fe atoms, causing more structure defects in the ferrite nanozyme and more active

https://doi.org/10.1021/acs.langmuir.2c00657
Langmuir 2022, 38, 8266−8279

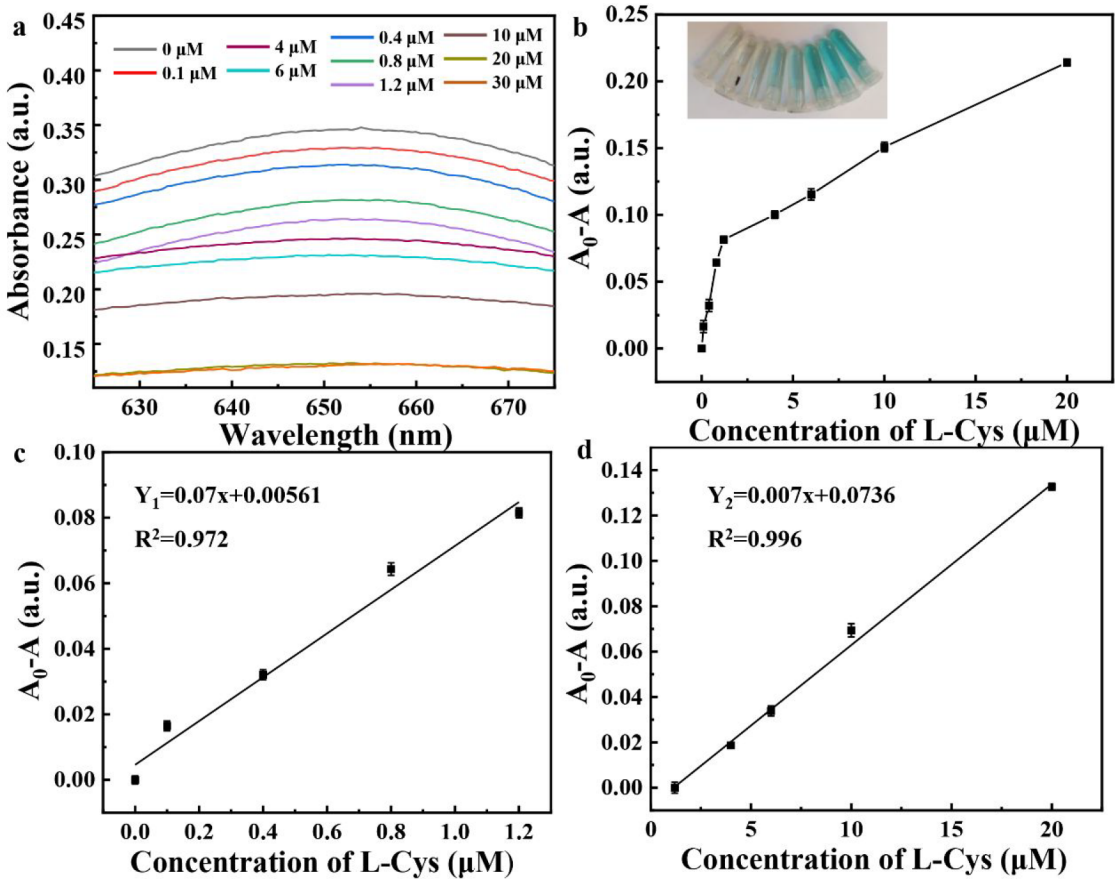

Figure 6. L-Cys sensing platform constructed by ferrite nanozyme. (a) Visible light absorption curves of the detection system containing ferrite nanozyme (50 mg L^{-1}), TMB (0.1 mM), H_2O_2 (1 mM), and L-Cys with different concentrations at pH 3.6. (b) Absorption evolution at 652 nm in the detection system when increasing the L-Cys concentrations. Inset: photographs of absorption turnoff in the detection system when increasing the L-Cys concentrations. (c, d) Independent linear calibration plots for L-Cys sensing in the ranges 0.2−1.2 and 1.2−20 μM, where A_0 and A are the absorbance at 652 nm in the absence and presence of L-Cys.

catalytic sites.[79] The detailed mechanism is not fully understood, but a combination of surface defects, polarization, and surface charge seems to be the most plausible reason for observation of low K_m.

L-Cys Detection Based on the Ferrite Nanozyme as the Sensing Platform. L-Cys can participate in the reduction process of cells and the metabolism of phospholipids in the liver. It can not only protect hepatocytes from damage but also restore liver function and promote the detoxification effect of the liver.[80−82] Thus, the construction of facile and efficient methods of detecting trace L-Cys has subsequently attracted considerable attention. L-Cys can be regarded as a reductant to convert the ox-TMB to TMB.[83] As illustrated in Figure 6a, the TMB substrate can be catalyzed by the ferrite nanozyme in the presence of H_2O_2, generating a blue ox-TMB with intensive absorption at 652 nm. A colorless solution appeared, and no absorption can be detected when the L-Cys was introduced into the detection system. According to the above-mentioned inhibition effect of L-Cys toward the TMB oxidation, a feasible colorimetric detection method is established to both qualitatively and quantitatively analyze the L-Cys contents by a mixing-and-detecting protocol. In the preferred detection systems, the sensitivity of the L-Cys sensing method is evaluated by mixing the targets with TMB, H_2O_2, and ferrite nanozyme. The absorption at 652 nm is gradually decreased when increasing the L-Cys dosage (Table S7 and Figure 6a,b). Furthermore, the color change of the detection systems with different contents of L-Cys is clearly distinguished on visual observation (inset in Figure 6b). Thus, the ferrite nanozyme-based sensing platform offers a reliable way to conduct the visual analysis of L-Cys by the naked eye. It is worth noting that the absorbance reaches a lowest value when the L-Cys concentration is 20 μM on account of the complete reduction of the oxidized substance by excessive L-Cys. As presented in Figure 6c,d, the data exhibit two linear relationships between L-Cys concentration and absorbance at 652 nm: Y1 = 0.07x + 0.0056 when the L-Cys concentration increases from 0.2 to 1.2 μM (R^2 = 0.97) and Y2 = 0.007x + 0.074 when the L-Cys concentration increases from 1.2 to 20 μM (R^2 = 0.99). The LOD of the L-Cys is calculated to be 0.119 μM based on the 3σ/slope role, which is at a relatively low level compared with previous colorimetric detection of L-Cys by nanozymes (Table 1).[37,47−54]

Turnoff Mechanism of L-Cys in the Ferrite Nanozyme−Hydrogen Peroxide−TMB System. As for the high-sensitivity response, the detection principle at the molecular level is analyzed. The first thing to know is that both TMB and L-Cys can be oxidized by ·OH as demonstrated in eqs 7 and 8. Meanwhile, the L-Cys as a reductant can probably convert the ox-TMB into TMB. Therefore, the presence of a trace amount L-Cys can interfere with the H_2O_2-mediated oxidation of TMB to form ox-TMB. On the basis of the above transformation relationship among TMB, H_2O_2, ferrite nanozyme, and L-Cys,

https://doi.org/10.1021/acs.langmuir.2c00657
Langmuir 2022, 38, 8266−8279

Table 1. Comparison of Linear Range and LOD toward Colorimetric Detection of L-Cys by Nanozymes

peroxidase-like nanozymes	linear range (μM)	LOD (μM)	ref
reduced graphene oxide derivative	2−30	0.1	37
Fe_3O_4 magnetic nanoparticles	0−50	0.97	47
nickel oxide nanoflowers	20−100	1.1	48
$CuMnO_2$ nanoflakes	25−300	11.26	49
cobalt sulfide nanosheets	0.2−100	2.7	50
vanadium tetrasulfide	50−300	5.0	51
CeO_2/CoO	5−10	3.71	52
MoS_2−Au@Pt	4.8−38.4	0.7	53
Cu@Au(Ag)/Pt	0−0.4 mM and 0.4−3 mM	4	54
ferrite nanozyme	0.2−20	0.119	this work

two possible reaction paths can be deduced in the absorption turnoff as follows (Figure 7a). Path one is conducted by the ox-TMB production in the TMB−H_2O_2−ferrite nanozyme ternary system, and the L-Cys dominated the absorption turnoff process of reducing the blue ox-TMB into colorless TMB (eq 7). Path two is composed of the L-Cys-initiated neutralization of ·OH produced in the H_2O_2−ferrite nanozyme binary system and the oxidation of TMB to generate ox-TMB by the residual ·OH (eq 8). Results in Figure 7b show that the absorbance at 652 nm in the ternary system of the TMB−H_2O_2−ferrite nanozyme is 0.49 after reaction for 60 min to realize the complete oxidation of TMB. When the L-Cys solution is added into the above mixture, the absorbance presents a dramatic decrease to 0.05 within 1 min, confirming that the L-Cys as a reductant can quickly convert the ox-TMB to TMB. Results in Figure 7c demonstrate that the reaction system eventually possesses negligible absorbance at 652 nm when the L-Cys is introduced into the binary H_2O_2−ferrite nanozyme in the early stage, whereas, the reaction system finally presents strong absorbance at 652 nm without the L-Cys addition into the binary H_2O_2−ferrite nanozyme in the early stage. The above phenomenon reveals that the L-Cys as a reductant can eliminate the ·OH and inhibit the generation of ox-TMB. The ·OH can be captured by DMPO to produce the DMPO−·OH adduct, which can be detected by EPR measurement. Results in Figure 7d indicate the four strong characteristic peaks of the DMPO−·OH adduct in the mixture of ferrite nanozyme + H_2O_2 + DMPO, whose intensity ratio is observed as 1:2:2:1.[85,86] However, there is no obvious EPR signal peak in the signals of neat H_2O_2. These shreds of evidence testify that the ferrite nanozyme can effectively convert H_2O_2 into ·OH. However, the intensities of four strong characteristic peaks are dramatically decreased after the L-Cys addition, further demonstrating the hydroxyl radical elimination by L-Cys.

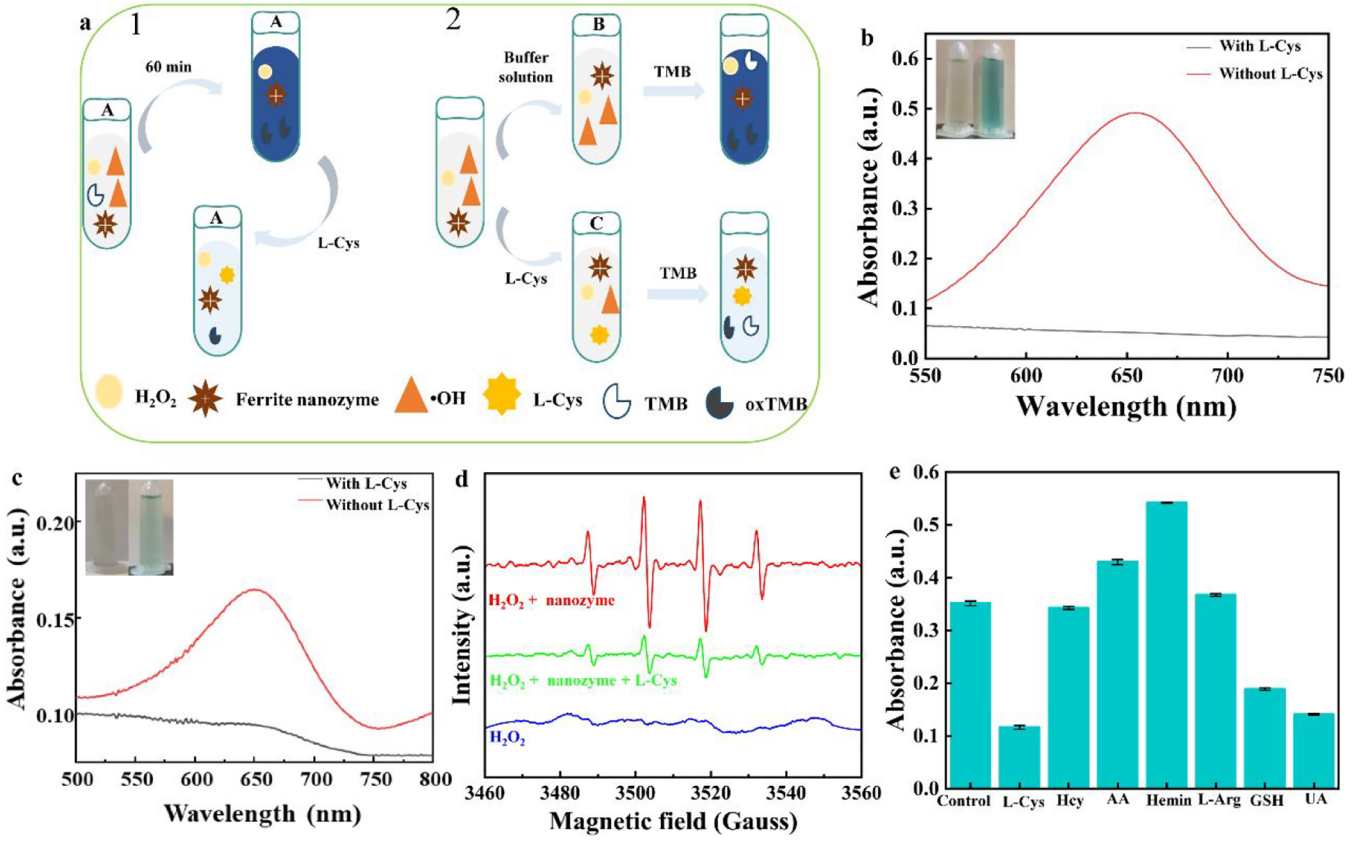

Figure 7. Turnoff mechanism of L-Cys in the ferrite nanozyme−hydrogen peroxide−TMB system. (a) Schematic diagram of experimental steps for verification of L-Cys detection mechanisms. (b) and (c) are the results of path 1 and path 2, respectively. The inset images visually indicate the amounts of the produced ox-TMB. (d) EPR assays of three systems (H_2O_2, H_2O_2 + nanozyme, and H_2O_2 + nanozyme + L-Cys). (e) Visible light absorption at 652 nm wavelength of ferrite nanozyme (50 mg L^{-1}) with the TMB (1 mM) and H_2O_2 (10 mM) systems in the presence of L-Cys and six other substances in serum, where concentrations of L-Cys and Hcy are 20 μM and the concentrations of other substances (AA, UA, hemin, L-Arg, and GSH) are 1 mM.

https://doi.org/10.1021/acs.langmuir.2c00657
Langmuir 2022, 38, 8266−8279

$$\mathrm{H_2O_2} \xrightarrow{\text{Ferrite nanozyme}} \cdot\mathrm{OH}$$
$$\mathrm{TMB} + \cdot\mathrm{OH} \longrightarrow \mathrm{oxTMB} \quad (7)$$
$$\text{L-Cys} + \mathrm{oxTMB} \longrightarrow \mathrm{TMB} + \text{Cys-Cys}$$

$$\mathrm{H_2O_2} \xrightarrow{\text{Ferrite nanozyme}} \cdot\mathrm{OH}$$
$$\text{L-Cys} + \cdot\mathrm{OH} \longrightarrow \text{Cys-Cys} \quad (8)$$
$$\mathrm{TMB} + \cdot\mathrm{OH} \longrightarrow \mathrm{oxTMB}$$

The selectivity of the L-Cys detection based on the peroxidase-mimicking activity of the ferrite nanozyme is studied by screening its response to biological targets. Several biological small molecules possessing similar molecular structure with L-Cys or reducibility are selected to study their interference effect on this method (Figure 7e). The concentrations of L-Cys and Hcy are set to be 20 μM, corresponding to the maximum detection concentration in the linear equation in Figure 6e. The concentrations of AA, UA, GSH, hemin, and arginine are fixed at 1 mM, whose concentrations are 50 times that of L-Cys. It should be noted that the concentrations of the AA, UA, GSH, hemin, and arginine are set at such an ultrahigh level to strengthen their effect on the detection reaction. The concentration of Hcy is set to be the same as that of L-Cys because of its limited solubility in the aqueous phase. A control experiment consisting of H_2O_2, ferrite nanozyme, and TMB is first conducted as a reference standard, presenting an absorbance of about 0.35. The addition of L-Cys into the ternary H_2O_2–ferrite nanozyme–TMB system leads to an obvious absorbance decrease from 0.35 to 0.1, matching the results in Figure. 6. Meanwhile, the high concentration addition of AA, UA, and GSH only shows a slight absorbance decrease, which is probably caused by their lower affinity with the substances in the detection system or the lower reducibility compared with the L-Cys. The equal concentration addition of Hcy hardly causes an absorbance decrease, revealing a low detection selectivity for Hcy. On the contray, the high concentration addition of hemin and arginine even presents an abnormal increase, which is possibly a result of their oxidability to facilitate the generation of ox-TMB. The above results suggest that the selectivity of the ferrite nanozyme-based sensing system is quite acceptable.

Detection of L-Cys in Real Samples by Using the Ferrite Nanozyme. To evaluate the practical applicability of the proposed method for L-Cys detection in real samples, the ferrite nanozyme is used for the determination of L-Cys in human blood serum. The human blood serum samples are collected from the nearby clinical laboratory and diluted 10 times with buffer solution (pH 3.6). Considering the difference of L-Cys concentrations in different serum samples, the concentrations of three diluted samples are determined based on the linear eq 1, which are 0.53, 0.82, and 0.99 μM, respectively (Tables S8 and 1). Similarly, other diluted samples with higher concentrations (>1 μM) are analyzed with the assistance of the linear eq 2, whose concentrations are also listed in Tables S8 and 1.

Recovery tests are also employed to estimate the accuracy of the as proposed method by standard addition method. First, a L-Cys solution with an exact concentration is added in the real samples. Then, the spiked concentrations of L-Cys in the samples are determined according to the linear equations in Figure 6. The corresponding results are obtained and shown in Table 2. The recoveries of the spiked samples are in the range

Table 2. Analysis of Human Serum Sample with the Proposed Colorimetric Assay

sample	concn (μM)	spiked concn (μM)	recovery (%)	RSD (%)
1	0.53	1.23	99.8	5.32
2	0.82	1.53	102.3	4.28
3	0.99	1.66	95.6	3.13
4	8.70	9.46	108.4	2.89
5	14.01	14.69	97.2	1.57
6	17.94	18.68	104.8	3.49
7	11.46	12.15	98.3	5.21
8	12.85	13.52	95.2	4.11

95.2%–108.4%, which suggests that the present method can be employed for the detection of L-Cys in real samples. The RSD values are calculated to be <10%, which are comparable to those previously reported works.[36,84,87−89] These results demonstrate the satisfactory reproducibility and applicability of this novel ferrite nanozyme for L-Cys monitoring in biological samples.

CONCLUSIONS

In summary, ferrite nanocrystals with excellent peroxidase-like activity are prepared by a facile two-step of continuous flow coprecipitation and high-temperature annealing. Comprehensive analysis has demonstrated that the proposed ferrite nanocrystals can effectively catalyze the oxidation of colorimetric substrate of TMB in the presence of H_2O_2 and present the concentration and pH dependence of the peroxidase performances. This fascinating characteristic stems from their ability to decompose of H_2O_2 into ·OH. A facile colorimetric method for L-Cys quantitative detection is established by employing the ferrite nanocrystal-based enzyme mimics as the sensing platform. The detailed mechanism of absorption turnoff in the L-Cys detection is determined to be the reduction of ·OH and ox-TMB by L-Cys. The proposed investigation not only demonstrates a new strategy for creating highly active and specific peroxidase mimics but also provides versatile opportunities for the establishment of nanozyme-based biosensors in the fields of bioanalytical chemistry and point-of-care testing.

ASSOCIATED CONTENT

Supporting Information

The Supporting Information is available free of charge at https://pubs.acs.org/doi/10.1021/acs.langmuir.2c00657.

EDX analysis of the element composition of the ferrite nanozyme; element composition of ferrite nanozyme; full-survey-scan spectrum of the ferrite nanozyme sample; visible light absorption spectra of ferrite nanoenzyme in the wavelength range 500–800 nm under different pH; gradually deepened color of dispersion containing TMB and H_2O_2 along with the increased concentration of ferrite nanozyme from 0 to 50 mg L^{-1}; data for pH-dependent POD activity of the ferrite nanozyme; changing color of dispersion containing fixed contents of ferrite nanozyme, TMB, and H_2O_2 along with the increased pH condition from 2.8 to 7; values of TMB concentration and velocity for the calculation of K_m and

https://doi.org/10.1021/acs.langmuir.2c00657
Langmuir 2022, 38, 8266−8279

V_{max}; data for establishing Lineweaver−Burk equation with TMB as substrate; values of H_2O_2 concentration and velocity for the calculation of K_m and V_{max}; data for establishing the Lineweaver−Burk equation with H_2O_2 as substrate; zeta potential of the binary ferrite nanozyme−TMB dispersion; values of L-Cys concentration and absorbance at 652 nm for establishing the linear equations of L-Cys detection; data for L-Cys detection in human serum sample (PDF)

AUTHOR INFORMATION

Corresponding Authors

Pengcheng Lin − *Guangdong Provincial Key Laboratory on Functional Soft Condensed Matter, Materials and Energy School, Guangdong University of Technology Panyu District, Guangzhou 510006, China;* orcid.org/0000-0002-1272-7982; Email: pclin@gdut.edu.cn

Wei Xiao − *Department of Laboratory Medicine, Guangdong Second Provincial General Hospital, Guangzhou 510317, China*; Email: xkevent@foxmail.com

Donglin Cao − *Department of Laboratory Medicine, Guangdong Second Provincial General Hospital, Guangzhou 510317, China*; Email: caodl@126.com

Authors

Hongjiao Wu − *Guangdong Provincial Key Laboratory on Functional Soft Condensed Matter, Materials and Energy School, Guangdong University of Technology Panyu District, Guangzhou 510006, China; Department of Laboratory Medicine, Guangdong Second Provincial General Hospital, Guangzhou 510317, China*

Jun Liu − *Guangdong Provincial Key Laboratory on Functional Soft Condensed Matter, Materials and Energy School, Guangdong University of Technology Panyu District, Guangzhou 510006, China*

Zhuoyu Chen − *Guangdong Provincial Key Laboratory on Functional Soft Condensed Matter, Materials and Energy School, Guangdong University of Technology Panyu District, Guangzhou 510006, China*

Wentao Ou − *Guangdong Provincial Key Laboratory on Functional Soft Condensed Matter, Materials and Energy School, Guangdong University of Technology Panyu District, Guangzhou 510006, China*

Zian Wang − *Guangdong Provincial Key Laboratory on Functional Soft Condensed Matter, Materials and Energy School, Guangdong University of Technology Panyu District, Guangzhou 510006, China*

Ying Chen − *Guangdong Provincial Key Laboratory on Functional Soft Condensed Matter, Materials and Energy School, Guangdong University of Technology Panyu District, Guangzhou 510006, China*

Complete contact information is available at: https://pubs.acs.org/10.1021/acs.langmuir.2c00657

Author Contributions

P.L., W.X., and D.C. designed the study. H.W. designed and performed experiments with the assistance of J.L., Z.C., W.O., Z.W., and Y.C. H.W. contributed to the writing of the manuscript and interpretation of data. All authors read and approved the final manuscript.

Notes

The authors declare no competing financial interest.

Availability of Data and Materials. All data generated or analyzed during this study are included in the article and additional file.

ACKNOWLEDGMENTS

The work was supported by the Science and Technology Projects in Guangzhou (202102080500), the Natural Science Foundation of Guangdong Province, China (Grant No. 2021A1515110712, 2021A1515220067), the Science Foundation of Guangdong Second Provincial General Hospital (Grant 3D-A2021003), Guangdong Provincial Key Laboratory of Point-of-care Testing (POCT) (Grant 2020B1111160004), the Guangdong Basic and Applied Basic Research Foundation (2019A1515011379), the Guangdong Special Support Program (2017TX04N371), and Guangdong Enterprise Sci-tech Commisioner (GDKTP2020013400).

REFERENCES

(1) Wagner, J.; Lerner, R. A.; Barbas, C. F. Efficient aldolase catalytic antibodies that use the enamine mechanism of natural enzymes. *Science* **1995**, *270* (5243), 1797−1800.

(2) Breaker, R. R. DNA enzymes. *Nat. Biotechnol.* **1997**, *15* (5), 427−431.

(3) Gioia, M.; Ciaccio, C.; Calligari, P.; De Simone, G.; Sbardella, D.; Tundo, G.; Fasciglione, G. F.; Di Masi, A.; Di Pierro, D.; Bocedi, A.; Ascenzi, P.; Coletta, M. Role of proteolytic enzymes in the COVID-19 infection and promising therapeutic approaches. *Biochem. Pharmacol.* **2020**, *182*, 114225.

(4) Planas-Iglesias, J.; Marques, S. M.; Pinto, G. P.; Musil, M.; Stourac, J.; Damborsky, J.; Bednar, D. Computational design of enzymes for biotechnological applications. *Biotechnol. Adv.* **2021**, *47*, 107696.

(5) Zhang, R.; Yan, X.; Fan, K. Nanozymes inspired by natural enzymes. *Acc. Mater. Res.* **2021**, *2* (7), 534−547.

(6) Ashrafi, A. M.; Bytesnikova, Z.; Barek, J.; Richtera, L.; Adam, V. A critical comparison of natural enzymes and nanozymes in biosensing and bioassays. *Biosens. Bioelectron* **2021**, *192*, 113494.

(7) Nanda, V.; Koder, R. L. Designing artificial enzymes by intuition and computation. *Nat. Chem.* **2010**, *2* (1), 15−24.

(8) Gao, L.; Zhuang, J.; Nie, L.; Zhang, J.; Zhang, Y.; Gu, N.; Wang, T.; Feng, J.; Yang, D.; Perrett, S.; Yan, X. Intrinsic peroxidase-like activity of ferromagnetic nanoparticles. *Nat. Nanotechnol.* **2007**, *2* (9), 577−583.

(9) Wei, H.; Gao, L.; Fan, K.; Liu, J.; He, J.; Qu, X.; Dong, S.; Wang, E.; Yan, X. Nanozymes: A clear definition with fuzzy edges. *Nano Today* **2021**, *40*, 101269.

(10) Wu, J.; Wei, H. Efficient design strategies for nanozymes. *Prog. Chem.* **2021**, *33* (1), 42.

(11) Wu, X.; Sun, Y.; He, T.; Zhang, Y.; Zhang, G.-J.; Liu, Q.; Chen, S. Iron, Nitrogen-doped carbon aerogels for fluorescent and electrochemical dual-mode detection of glucose. *Langmuir* **2021**, *37* (38), 11309−11315.

(12) Wang, J.; Yang, X.; Wei, T.; Bao, J.; Zhu, Q.; Dai, Z. Fe-Porphyrin-based covalent organic framework as a novel peroxidase mimic for a one-pot glucose colorimetric assay. *ACS Appl. Bio Mater.* **2018**, *1* (2), 382−388.

(13) Sun, S.; Zhang, Z.; Xiang, Y.; Cao, M.; Yu, D. Amino acid-mediated synthesis of the ZIF-8 nanozyme that reproduces both the zinc-coordinated active center and hydrophobic pocket of natural carbonic anhydrase. *Langmuir* **2022**, *38* (4), 1621−1630.

(14) Liu, Y.; Qing, Y.; Jing, L.; Zou, W.; Guo, R. Platinum−Copper Bimetallic Colloid Nanoparticle Cluster Nanozymes with Multiple Enzyme-like Activities for Scavenging Reactive Oxygen Species. *Langmuir* **2021**, *37* (24), 7364−7372.

(15) Shi, W.; Wang, Q.; Long, Y.; Cheng, Z.; Chen, S.; Zheng, H.; Huang, Y. Carbon nanodots as peroxidase mimetics and their applications to glucose detection. *Chem. Commun.* **2011**, *47* (23), 6695−6697.

(16) Lin, L.; Song, X.; Chen, Y.; Rong, M.; Zhao, T.; Wang, Y.; Jiang, Y.; Chen, X. Intrinsic peroxidase-like catalytic activity of nitrogen-

doped graphene quantum dots and their application in the colorimetric detection of H_2O2 and glucose. *Anal. Chim. Acta* **2015**, *869*, 89−95.
(17) Song, C.; Ding, W.; Zhao, W.; Liu, H.; Wang, J.; Yao, Y.; Yao, C. High peroxidase-like activity realized by facile synthesis of FeS2 nanoparticles for sensitive colorimetric detection of H_2O2 and glutathione. *Biosens. Bioelectron* **2020**, *151*, 111983.
(18) Ding, Y.; Liu, H.; Gao, L.-N.; Fu, M.; Luo, X.; Zhang, X.; Liu, Q.; Zeng, R.-C. Fe-doped Ag2S with excellent peroxidase-like activity for colorimetric determination of H_2O2. *J. Alloys Compd.* **2019**, *785*, 1189−1197.
(19) Li, M.; Chen, J.; Wu, W.; Fang, Y.; Dong, S. Oxidase-like MOF-818 nanozyme with high specificity for catalysis of catechol oxidation. *J. Am. Chem. Soc.* **2020**, *142* (36), 15569−15574.
(20) Ji, Y.; Gao, W.; Zhang, S.; Li, B.; Huang, H.; Zhang, X. Confining Natural/Mimetic Enzyme Cascade in an Amorphous Metal−Organic Framework for the Construction of Recyclable Biomaterials with Catalytic Activity. *Langmuir* **2022**, *38* (3), 927−936.
(21) Wu, X.; Chen, T.; Chen, Y.; Yang, G. Modified Ti_3C_2 nanosheets as peroxidase mimetics for use in colorimetric detection and immunoassays. *J. Mater. Chem. B* **2020**, *8* (13), 2650−2659.
(22) Liu, Y.; Ding, D.; Zhen, Y.; Guo, R. Amino acid-mediated 'turn-off/turn-on'nanozyme activity of gold nanoclusters for sensitive and selective detection of copper ions and histidine. *Biosens. Bioelectron* **2017**, *92*, 140−146.
(23) Wang, G.-L.; Jin, L.-Y.; Dong, Y.-M.; Wu, X.-M.; Li, Z.-J. Intrinsic enzyme mimicking activity of gold nanoclusters upon visible light triggering and its application for colorimetric trypsin detection. *Biosens. Bioelectron* **2015**, *64*, 523−529.
(24) Xu, L.; Wang, J.; Lu, S.-Y.; Wang, X.; Cao, Y.; Wang, M.; Liu, F.; Kang, Y.; Liu, H. Construction of a polypyrrole-based multifunctional nanocomposite for dual-modal imaging and enhanced synergistic phototherapy against cancer cells. *Langmuir* **2019**, *35* (28), 9246−9254.
(25) Cormode, D. P.; Gao, L.; Koo, H. Emerging biomedical applications of enzyme-like catalytic nanomaterials. *Trends Biotechnol* **2018**, *36* (1), 15−29.
(26) Ganganboina, A. B.; Doong, R.-A. The biomimic oxidase activity of layered V2O5 nanozyme for rapid and sensitive nanomolar detection of glutathione. *Sens. Actuators, B* **2018**, *273*, 1179−1186.
(27) Vernekar, A. A.; Das, T.; Ghosh, S.; Mugesh, G. A remarkably efficient MnFe2O4-based oxidase nanozyme. *Chem.—Asian J.* **2016**, *11* (1), 72−76.
(28) He, W.; Zhou, Y.-T.; Wamer, W. G.; Hu, X.; Wu, X.; Zheng, Z.; Boudreau, M. D.; Yin, J.-J. Intrinsic catalytic activity of Au nanoparticles with respect to hydrogen peroxide decomposition and superoxide scavenging. *Biomaterials* **2013**, *34* (3), 765−773.
(29) Moglianetti, M.; De Luca, E.; Pedone, D.; Marotta, R.; Catelani, T.; Sartori, B.; Amenitsch, H.; Retta, S. F.; Pompa, P. P. Platinum nanozymes recover cellular ROS homeostasis in an oxidative stress-mediated disease model. *Nanoscale* **2016**, *8* (6), 3739−3752.
(30) Zhang, H.; Han, Y.; Yang, Y.; Chen, J.; Qiu, H. Construction of a Carbon Dots/Cobalt Oxyhydroxide Nanoflakes Biosensing Platform for Detection of Acid Phosphatase. *Langmuir* **2021**, *37* (35), 10529−10537.
(31) Wang, H.; Li, P.; Yu, D.; Zhang, Y.; Wang, Z.; Liu, C.; Qiu, H.; Liu, Z.; Ren, J.; Qu, X. Unraveling the enzymatic activity of oxygenated carbon nanotubes and their application in the treatment of bacterial infections. *Nano Lett.* **2018**, *18* (6), 3344−3351.
(32) Hu, Y.; Cheng, H.; Zhao, X.; Wu, J.; Muhammad, F.; Lin, S.; He, J.; Zhou, L.; Zhang, C.; Deng, Y.; Wang, P.; Zhou, Z.; Nie, S.; Wei, H. Surface-enhanced Raman scattering active gold nanoparticles with enzyme-mimicking activities for measuring glucose and lactate in living tissues. *ACS Nano* **2017**, *11* (6), 5558−5566.
(33) Huang, Y.; Zhao, M.; Han, S.; Lai, Z.; Yang, J.; Tan, C.; Ma, Q.; Lu, Q.; Chen, J.; Zhang, X.; Zhang, Z.; Li, B.; Chen, B.; Zong, Y.; Zhang, H. Growth of au nanoparticles on 2D metalloporphyrinic metal-organic framework nanosheets used as biomimetic catalysts for cascade reactions. *Adv. Mater.* **2017**, *29* (32), 1700102.
(34) Hou, C.; Wang, Y.; Ding, Q.; Jiang, L.; Li, M.; Zhu, W.; Pan, D.; Zhu, H.; Liu, M. Facile synthesis of enzyme-embedded magnetic metal−organic frameworks as a reusable mimic multi-enzyme system: mimetic peroxidase properties and colorimetric sensor. *Nanoscale* **2015**, *7* (44), 18770−18779.
(35) Bao, Y.-W.; Hua, X.-W.; Ran, H.-H.; Zeng, J.; Wu, F.-G. Metal-doped carbon nanoparticles with intrinsic peroxidase-like activity for colorimetric detection of H_2O_2 and glucose. *J. Mater. Chem. B* **2019**, *7* (2), 296−304.
(36) Dega, N. K.; Ganganboina, A. B.; Tran, H. L.; Kuncoro, E. P.; Doong, R.-A. BSA-stabilized manganese phosphate nanoflower with enhanced nanozyme activity for highly sensitive and rapid detection of glutathione. *Talanta* **2022**, *237*, 122957.
(37) Liu, C.; Zhao, Y.; Xu, D.; Zheng, X.; Huang, Q. A green and facile approach to a graphene-based peroxidase-like nanozyme and its application in sensitive colorimetric detection of l-cysteine. *Anal. Bioanal. Chem.* **2021**, *413* (15), 4013−4022.
(38) Gao, L.; Gao, X.; Yan, X. Kinetics and mechanisms for nanozymes. *Nanozymology* **2020**, 17−39.
(39) Ji, S.; Jiang, B.; Hao, H.; Chen, Y.; Dong, J.; Mao, Y.; Zhang, Z.; Gao, R.; Chen, W.; Zhang, R.; et al. Matching the kinetics of natural enzymes with a single-atom iron nanozyme. *Nat. Catal* **2021**, *4* (5), 407−417.
(40) Wu, J.; Lv, W.; Yang, Q.; Li, H.; Li, F. Label-free homogeneous electrochemical detection of MicroRNA based on target-induced anti-shielding against the catalytic activity of two-dimension nanozyme. *Biosens. Bioelectron* **2021**, *171*, 112707.
(41) Nagvenkar, A. P.; Gedanken, A. Cu0. 89Zn0. 11O, a new peroxidase-mimicking nanozyme with high sensitivity for glucose and antioxidant detection. *ACS Appl. Mater. Interfaces* **2016**, *8* (34), 22301−22308.
(42) Liu, Y.; Zhou, M.; Cao, W.; Wang, X.; Wang, Q.; Li, S.; Wei, H. Light-responsive metal−organic framework as an oxidase mimic for cellular glutathione detection. *Anal. Chem.* **2019**, *91* (13), 8170−8175.
(43) Qin, F.-X.; Jia, S.-Y.; Wang, F.-F.; Wu, S.-H.; Song, J.; Liu, Y. Hemin@ metal−organic framework with peroxidase-like activity and its application to glucose detection. *Catal. Sci. Technol.* **2013**, *3* (10), 2761−2768.
(44) Li, Z.; Wang, Y.; Ni, Y.; Kokot, S. A rapid and label-free dual detection of Hg (II) and cysteine with the use of fluorescence switching of graphene quantum dots. *Sens. Actuators, B* **2015**, *207*, 490−497.
(45) Gong, T.; Liu, J.; Liu, X.; Liu, J.; Xiang, J.; Wu, Y. A sensitive and selective sensing platform based on CdTe QDs in the presence of L-cysteine for detection of silver, mercury and copper ions in water and various drinks. *Food Chem.* **2016**, *213*, 306−312.
(46) Huang, H.; Weng, Y.; Zheng, L.; Yao, B.; Weng, W.; Lin, X. Nitrogen-doped carbon quantum dots as fluorescent probe for "off-on" detection of mercury ions, L-cysteine and iodide ions. *J. Colloid Interface Sci.* **2017**, *506*, 373−378.
(47) Wu, X.-Q.; Xu, Y.; Chen, Y.-L.; Zhao, H.; Cui, H.-J.; Shen, J.-S.; Zhang, H.-W. Peroxidase-like activity of ferric ions and their application to cysteine detection. *RSC Adv.* **2014**, *4* (110), 64438−64442.
(48) Ray, C.; Dutta, S.; Sarkar, S.; Sahoo, R.; Roy, A.; Pal, T. Intrinsic peroxidase-like activity of mesoporous nickel oxide for selective cysteine sensing. *J. Mater. Chem. B* **2014**, *2* (36), 6097−6105.
(49) Chen, Y.; Chen, T.; Wu, X.; Yang, G. CuMnO2 nanoflakes as pH-switchable catalysts with multiple enzyme-like activities for cysteine detection. *Sens. Actuators, B* **2019**, *279*, 374−384.
(50) Hashmi, S.; Singh, M.; Weerathunge, P.; Mayes, E. L. H.; Mariathomas, P. D.; Prasad, S. N.; Ramanathan, R.; Bansal, V. Cobalt Sulfide Nanosheets as Peroxidase Mimics for Colorimetric Detection of l-Cysteine. *ACS Appl. Nano Mater.* **2021**, *4* (12), 13352−13362.
(51) Chen, C.; Wang, Y.; Zhang, D. Peroxidase-like activity of vanadium tetrasulfide submicrospheres and its application to the colorimetric detection of hydrogen peroxide and L-cysteine. *Microchim. Acta* **2019**, *186* (12), 1−8.
(52) Lian, J.; Liu, P.; Jin, C.; Liu, Q.-Y.; Zhang, X.; Zhang, X. Flower-like CeO_2/CoO p−n heterojuncted nanocomposites with enhanced

https://doi.org/10.1021/acs.langmuir.2c00657
Langmuir 2022, 38, 8266−8279

peroxidase-mimicking activity for l-cysteine sensing. *ACS Sustainable Chem. Eng.* **2020**, *8* (47), 17540−17550.
(53) Wan, L.; Wu, L.; Su, S.; Zhu, D.; Chao, J.; Wang, L. High peroxidase-mimicking activity of gold@ platinum bimetallic nanoparticle-supported molybdenum disulfide nanohybrids for the selective colorimetric analysis of cysteine. *Chem. Commun.* **2020**, *56* (82), 12351−12354.
(54) Jiang, C.; Wei, X.; Bao, S.; Tu, H.; Wang, W. Cu@ Au (Ag)/Pt nanocomposite as peroxidase mimic and application of Cu@ Au/Pt in colorimetric detection of glucose and l-cysteine. *RSC Adv.* **2019**, *9* (71), 41561−41568.
(55) Yu, Z.; Lou, R.; Pan, W.; Li, N.; Tang, B. Nanoenzymes in disease diagnosis and therapy. *Chem. Commun.* **2020**, *56*, 15513.
(56) Wang, L.; Miao, L.; Yang, H.; Yu, J.; Xie, Y.; Xu, L.; Song, Y. A novel nanoenzyme based on Fe_3O_4 nanoparticles@ thionine-imprinted polydopamine for electrochemical biosensing. *Sens. Actuators, B* **2017**, *253*, 108−114.
(57) Lyu, M.; Zhu, D.; Kong, X.; Yang, Y.; Ding, S.; Zhou, Y.; Quan, H.; Duo, Y.; Bao, Z. Glutathione-Depleting Nanoenzyme and Glucose Oxidase Combination for Hypoxia Modulation and Radiotherapy Enhancement. *Adv. Healthcare Mater.* **2020**, *9* (11), 1901819.
(58) Mei, X.; Hu, T.; Wang, H.; Liang, R.; Bu, W.; Wei, M. Highly dispersed nano-enzyme triggered intracellular catalytic reaction toward cancer specific therapy. *Biomaterials* **2020**, *258*, 120257.
(59) Wei, W.; Cui, X.; Chen, W.; Ivey, D. G. Phase-controlled synthesis of MnO2 nanocrystals by anodic electrodeposition: implications for high-rate capability electrochemical supercapacitors. *J. Phys. Chem. C* **2008**, *112* (38), 15075−15083.
(60) Xia, H.; Feng, J.; Wang, H.; Lai, M. O.; Lu, L. MnO2 nanotube and nanowire arrays by electrochemical deposition for supercapacitors. *J. Power Sources* **2010**, *195* (13), 4410−4413.
(61) Moura, K.; Lima, R.; Coelho, A.; Souza-Junior, E.; Duque, J.; Meneses, C. Tuning the surface anisotropy in Fe-doped NiO nanoparticles. *Nanoscale* **2014**, *6* (1), 352−357.
(62) Liang, R.; Shen, L.; Jing, F.; Qin, N.; Wu, L. Preparation of MIL-53 (Fe)-reduced graphene oxide nanocomposites by a simple self-assembly strategy for increasing interfacial contact: efficient visible-light photocatalysts. *ACS Appl. Mater. Interfaces* **2015**, *7* (18), 9507−9515.
(63) Lv, H.; Zhao, H.; Cao, T.; Qian, L.; Wang, Y.; Zhao, G. Efficient degradation of high concentration azo-dye wastewater by heterogeneous Fenton process with iron-based metal-organic framework. *J. Mol. Catal. A: Chem.* **2015**, *400*, 81−89.
(64) Xia, H.; Zhu, D.; Luo, Z.; Yu, Y.; Shi, X.; Yuan, G.; Xie, J. Hierarchically structured Co3O4@Pt@MnO2 nanowire arrays for high-performance supercapacitors. *Sci. Rep* **2013**, *3* (1), 1−8.
(65) Lei, K.; Han, X.; Hu, Y.; Liu, X.; Cong, L.; Cheng, F.; Chen, J. Chemical etching of manganese oxides for electrocatalytic oxygen reduction reaction. *Chem. Commun.* **2015**, *51* (58), 11599−11602.
(66) Xie, Q.; Liu, P.; Zeng, D.; Xu, W.; Wang, L.; Zhu, Z. Z.; Mai, L.; Peng, D. L. Dual electrostatic assembly of graphene encapsulated nanosheet-assembled ZnO-Mn-C hollow microspheres as a lithium ion battery anode. *Adv. Funct. Mater.* **2018**, *28* (19), 1707433.
(67) Dubale, A. A.; Pan, C.-J.; Tamirat, A. G.; Chen, H.-M.; Su, W.-N.; Chen, C.-H.; Rick, J.; Ayele, D. W.; Aragaw, B. A.; Lee, J.-F.; Yang, Y.-W.; Hwang, B.-J. Heterostructured Cu 2 O/CuO decorated with nickel as a highly efficient photocathode for photoelectrochemical water reduction. *J. Mater. Chem. A* **2015**, *3* (23), 12482−12499.
(68) Zhang, Q.; Huang, L.; Kang, S.; Yin, C.; Ma, Z.; Cui, L.; Wang, Y. CuO/Cu 2 O nanowire arrays grafted by reduced graphene oxide: synthesis, characterization, and application in photocatalytic reduction of CO 2. *RSC Adv.* **2017**, *7* (69), 43642−43647.
(69) Yang, J.; Zeng, D.; Zheng, H.; Xie, Q.; Huang, J.; Xiao, L.; Peng, D.-L. 3D graphene encapsulated ZnO-NiO-CuO double-shelled hollow microspheres with enhanced lithium storage properties. *J. Alloys Compd.* **2018**, *765*, 1158−1166.
(70) Meng, X.; Li, D.; Chen, L.; He, H.; Wang, Q.; Hong, C.; He, J.; Gao, X.; Yang, Y.; Jiang, B.; Nie, G.; Yan, X.; Gao, L.; Fan, K. High-Performance Self-Cascade Pyrite Nanozymes for Apoptosis−Ferroptosis Synergistic Tumor Therapy. *ACS Nano* **2021**, *15* (3), 5735−5751.
(71) Zhang, L.; Liu, Z.; Deng, Q.; Sang, Y.; Dong, K.; Ren, J.; Qu, X. Nature-Inspired Construction of MOF@ COF Nanozyme with Active Sites in Tailored Microenvironment and Pseudopodia-Like Surface for Enhanced Bacterial Inhibition. *Angew. Chem. Int. Ed* **2021**, *60* (7), 3469−3474.
(72) Xu, W.; Jiao, L.; Wu, Y.; Hu, L.; Gu, W.; Zhu, C. Metal−Organic Frameworks Enhance Biomimetic Cascade Catalysis for Biosensing. *Adv. Mater.* **2021**, *33* (22), 2005172.
(73) Miao, W.; Liu, Y.; Chen, X.; Zhao, Y.; Mao, S. Tuning layered Fe-doped g-C3N4 structure through pyrolysis for enhanced Fenton and photo-Fenton activities. *Carbon* **2020**, *159*, 461−470.
(74) Grebennikova, O.; Sviridova, I.; Matveeva, V.; Sulman, M. Magnetic nanoparticles in biocatalysis. *J. Phys.: Conf. Ser.* **2020**, 1658−012018.
(75) Liu, B.; Wang, Y.; Chen, Y.; Guo, L.; Wei, G. Biomimetic two-dimensional nanozymes: synthesis, hybridization, functional tailoring, and biosensor applications. *J. Mater. Chem. B* **2020**, *8* (44), 10065−10086.
(76) Ding, C.; Yan, Y.; Xiang, D.; Zhang, C.; Xian, Y. Magnetic Fe 3 S 4 nanoparticles with peroxidase-like activity, and their use in a photometric enzymatic glucose assay. *Microchim. Acta* **2016**, *183* (2), 625−631.
(77) Cai, S.; Liu, X.; Han, Q.; Qi, C.; Yang, R.; Wang, C. A novel strategy to construct supported Pd nanocomposites with synergistically enhanced catalytic performances. *Nano Res.* **2018**, *11* (6), 3272−3281.
(78) Zhang, Y.; Song, J.; Pan, Q.; Zhang, X.; Shao, W.; Zhang, X.; Quan, C.; Li, J. An Au@ NH 2-MIL-125 (Ti)-based multifunctional platform for colorimetric detections of biomolecules and Hg 2+. *J. Mater. Chem. B* **2020**, *8* (1), 114−124.
(79) Li, J.; Zhang, Y.; Zhang, X.; Huang, J.; Han, J.; Zhang, Z.; Han, X.; Xu, P.; Song, B. S. N dual-doped graphene-like carbon nanosheets as efficient oxygen reduction reaction electrocatalysts. *ACS Appl. Mater. Interfaces* **2017**, *9* (1), 398−405.
(80) Clemente Plaza, N.; Reig García-Galbis, M.; Martínez-Espinosa, R. M. Effects of the Usage of l-Cysteine (l-Cys) on Human Health. *Molecules* **2018**, *23* (3), 575.
(81) Saha, A.; Zhao, S.; Chen, Z.; Georgiou, G.; Stone, E.; Kidane, D.; DiGiovanni, J. Combinatorial Approaches to Enhance DNA Damage following Enzyme-Mediated Depletion of L-Cys for Treatment of Pancreatic Cancer. *Mol. Ther* **2021**, *29* (2), 775−787.
(82) Hou, C.; Fan, S.; Lang, Q.; Liu, A. Biofuel cell based self-powered sensing platform for L-cysteine detection. *Anal. Chem.* **2015**, *87* (6), 3382−3387.
(83) Zhang, T.; Li, H.; Liu, M.; Zhou, H.; Zhang, Z.; Yu, C.; Wang, C.; Wang, G. Improved the specificity of peroxidase-like carbonized polydopamine nanotubes with high nitrogen doping for glutathione detection. *Sens. Actuators, B* **2021**, *341*, 129987.
(84) Dong, W.; Wang, R.; Gong, X.; Liang, W.; Dong, C. A far-red FRET fluorescent probe for ratiometric detection of l-cysteine based on carbon dot40s and N-acetyl-l-cysteine-capped gold nanoparticles. *Spectrochim. Acta, Part A* **2019**, *213*, 90−96.
(85) Zhao, S.; Li, Y.; Liu, Q.; Li, S.; Cheng, Y.; Cheng, C.; Sun, Z.; Du, Y.; Butch, C. J.; Wei, H. An orally administered CeO_2@ montmorillonite nanozyme targets inflammation for inflammatory bowel disease therapy. *Adv. Funct. Mater.* **2020**, *30* (45), 2004692.
(86) Lou, Z.; Zhao, S.; Wang, Q.; Wei, H. N-doped carbon as peroxidase-like nanozymes for total antioxidant capacity assay. *Anal. Chem.* **2019**, *91* (23), 15267−15274.
(87) Sheng, J.; Jiang, X.; Wang, L.; Yang, M.; Liu, Y.-N. Biomimetic mineralization guided one-pot preparation of gold clusters anchored two-dimensional MnO2 nanosheets for fluorometric/magnetic bimodal sensing. *Anal. Chem.* **2018**, *90* (4), 2926−2932.
(88) Wang, Y.; Wang, D.; Sun, L.-H.; Zhang, L.-C.; Lu, Z.-S.; Xue, P.; Wang, F.; Xia, Q.-Y.; Bao, S.-J. BC@ DNA-Mn3 (PO4) 2 Nanozyme for Real-Time Detection of Superoxide from Living Cells. *Anal. Chem.* **2020**, *92* (24), 15927−15935.
(89) Peng, Y.; Yu, X.; Yin, W.; Dong, W.; Peng, J.; Wang, T. Colorimetric assay using mesoporous Fe-doped graphitic carbon

https://doi.org/10.1021/acs.langmuir.2c00657
Langmuir 2022, 38, 8266−8279

nitride as a peroxidase mimetic for the determination of hydrogen peroxide and glucose. *ACS Appl. Bio Mater.* **2020**, *3* (1), 59−67.

https://doi.org/10.1021/acs.langmuir.2c00657
Langmuir 2022, 38, 8266−8279